Article:
Carruthers, A.W., Shahmir, H., Hardwick, L. et al. (3 more authors) (2021) An assessment of the high-entropy alloy system VCrMnFeAlx. Journal of Alloys and Compounds, 888. 161525. ISSN 0925-8388

https://doi.org/10.1016/j.jallcom.2021.161525

Journal of Alloys and Compounds 888 (2021) 161525

Contents lists available at ScienceDirect

Journal of Alloys and Compounds

journal homepage: www.elsevier.com/locate/jalcom

An assessment of the high-entropy alloy system $VCrMnFeAl_x$

A.W. Carruthers[a,*], H. Shahmir[b], L. Hardwick[b], R. Goodall[b], A.S. Gandy[b], E.J. Pickering[a]

[a] Department of Materials, University of Manchester, Manchester M13 9PL, UK
[b] Department of Materials Science and Engineering, University of Sheffield, Sheffield S1 3JD, UK

ARTICLE INFO

Article history:
Received 25 March 2021
Received in revised form 28 June 2021
Accepted 9 August 2021
Available online 12 August 2021

Keywords:
Nuclear
Fussion
High entropy alloy
Low activation
TEM
SEM
EDX
HEA
VCrMnFe
VCrMnFeAl

ABSTRACT

A major consideration when choosing materials for nuclear reactors is the future radioactive waste produced by the irradiation of their component parts. Only a handful of structural metals can be considered 'low activation' in a fusion environment. In recent work, we showed that the low-activation multi-component equiatomic alloy VCrMnFe comprises a single BCC (A2) phase at 1200°C. Here, we examine its stability on ageing at lower temperatures, and the effect of Al additions (to create $VCrMnFeAl_x$ alloys) to destabilise the sigma phase and form strengthening superlattice structures. It is found that substantial volume fractions of sigma phase form after ageing VrCrMnFe at 600°C and 800°C for 1000 h. The addition of Al was found to destabilise the sigma phase, as predicted using thermodynamic modelling, with it being eliminated at all temperatures with additions of 6.6 at% Al. Increasing Al additions also led to the formation of superlattice structures: B2 and $L2_1$ (Heusler). Higher Al content had a slight increasing effect on the alloys' hardness, but also embrittled the alloys (at room temperature). Significant hardening was produced by nano-segregation induced in the higher Al x = 0.25, 0.5 and 1.0 alloys after aging at 600 °C. This alloy system presents an attractive opportunity to fine-tune the composition to obtain a balance of ductility and high-temperature strength and stability. Of particular interest was the formation a two-phase basket weave cube-on-cube orientated, coherent, microstructure in $VCrMnFeAl_{1.0}$ after aging at 800 °C.

1. Introduction

The potential number of element combinations for the construction of medium and high entropy alloys (HEAs) is incredibly large. However, there are considerations that can help narrow the field of study, e.g., if a solid solution is desired, then design criteria targeting this could be employed. On occasions, the elemental palette can be severely restricted by the end application being designed for, with a key example of this being a fusion reactor [1]. A major design consideration for fusion reactors is that the amount of active waste produced during the lifetime of the reactor is minimised. The FISPACT-II code [2] can be used to calculate the time it will take each element to cool to low-level waste after operation in a fusion reactor environment, as shown in the periodic table in Fig. 1. Eight elements considered to be most viable for the creation of low activation high entropy alloys (LAHEAs) are highlighted: Al, Ti, V, Cr, Mn, Fe, Ta, W. Other elements are ruled out due to their cost/scarcity, e.g., Au, or because they are typically only included in metallic alloys in relatively small quantities due to the generation of other phases, e.g. C and Si. This is not to state that any LAHEA is automatically suitable for operation in a nuclear reactor, rather, this is one important condition, and the motivation for the exploration of part of this compositional space in this study.

In our previous work [5], we investigated the quaternary equiatomic alloy TiVCrMnFe, which was found to contain a significant quantity of an undesirable, brittle intermetallic, C14 Laves phase even after annealing at high temperature (1200°C). Thus this alloy system is considered inappropriate for structural nuclear applications. However, it was also demonstrated that removal of the Ti from TiVCrMnFe, i.e., VCrMnFe, leads to the formation of a single-phase bcc solid solution at 1200 °C. It was recognised that C14 Laves phase is present in the binary phase diagrams of TiMn and TiFe. Other HEAs containing a significant number of Laves phases within the binary phase diagrams of their comprising elements have also shown significant volume fractions of Laves phase, or even single phase Laves phase [6,7]. It is noted that, in the case of single Laves phase alloys, the elements that sit on the A and B sites within the Laves phase are present in a similar ratio to that of Laves phase.

Using similar reasoning, as was also recognised in our previous work [5], within the six binary phase diagrams it is possible to make within the VCrMnFe system, sigma-phase is present in four of them at lower temperatures; VFe, CrFe, VMn, and CrMn [8]. The formation

* Corresponding author.
E-mail address: alexander.carruthers@manchester.ac.uk (A.W. Carruthers).

https://doi.org/10.1016/j.jallcom.2021.161525
0925-8388/

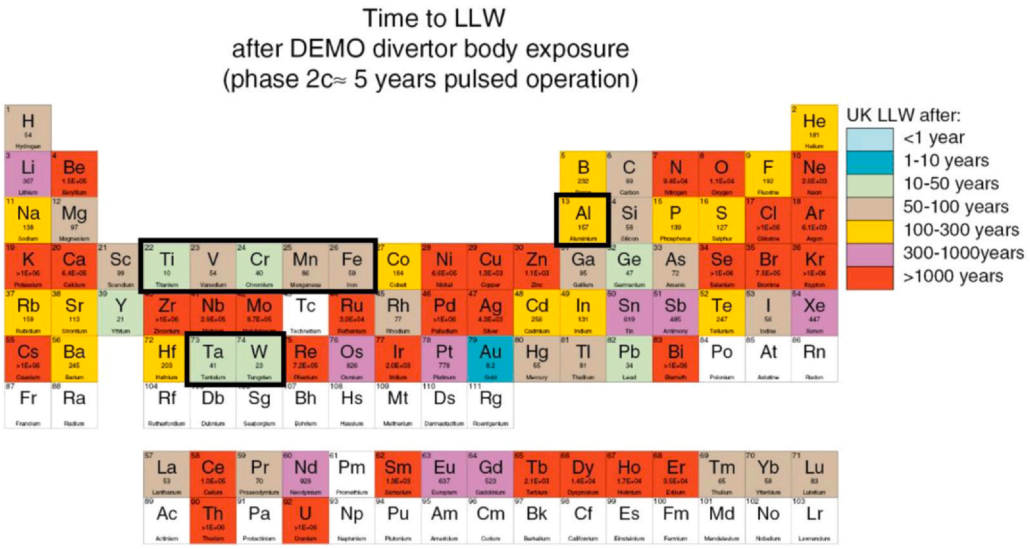

Fig. 1. Time required for each element to reach low-level activity waste (LLW) (UK low-level waste, < 4 MBq kg−1 alpha radiation and < 12 MBq kg−1 combined gamma and beta radiation) after ~5 years of pulsed operation in the DEMO nuclear reactor divertor body, as predicted by Gilbert et al. [3,4].

of large quantities of sigma phase would almost certainly be undesirable for structural applications. Hence, in the current work we aim to quantify the extent of sigma phase formation in VCrMnFe during ageing, and to examine the addition of a fifth element to suppress its formation.

The fifth element was chosen using a number of criteria: (i) that it must be metallic and solid at room temperature, (ii) decay to UK low-level waste following fusion reactor exposure in 100 years or less as per Fig. 1, (iii) must not be prohibitively expensive (Au, Pt group or rare earth), (iv) not highly toxic (As and Cd), and (v) must suppress the formation of sigma phase in the VCrMnFe system. Satisfaction of criterion (v) was determined by examining ternary phase diagrams with V or Cr in one corner, Fe or Mn in another, and the element of interest in the third. An element was considered viable if it reduced the compositional range over which sigma-phase was stable. This is outlined in Fig. 2. Only two elements satisfied all these criteria: Al [9,10] and Ga [11]. Al was chosen for this study as it has a higher melting temperature and lower density, Ga just barely satisfies criterion (i).

Introducing a fifth element to the alloy system may cause other phases to form. Al particularly is capable of forming several intermetallics in the binary systems with the other VCrMnFe alloying elements. Of particular note are phases based on an 'ordered BCC' structure, such as the B2 and Heusler ($L2_1$) intermetallics, both of which are common structures found within HEAs [12]. Furthermore, there are several ternary systems within the quinary VCrMnFeAl system that form Heusler phases, such as Fe_2VAl, Fe_2CrAl and Mn_2VAl [13–15]. All these B2 and Heusler compounds have the potential to act as superlattice strengthening precipitates. Thus, this paper examines how Al effects the formation of intermetallics within the VCrMnFe system, both with respect to sigma phase and to other ordered phases.

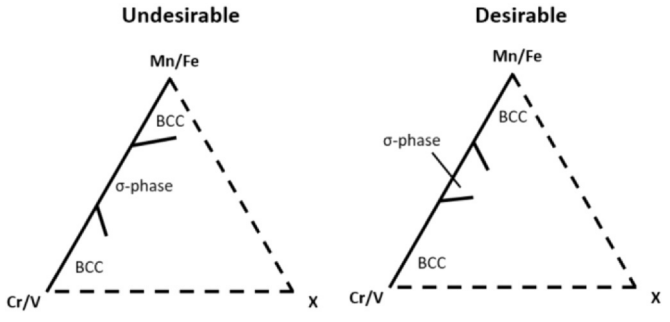

Fig. 2. Schematic of the search criteria of ternary phase diagrams.

The VCrMnFe quaternary was first aged at 600°C and 800°C to determine the extent of sigma phase precipitation. Then a suite of $VCrMnFeAl_x$ alloys were made with x = 0, 0.1, 0.2, 0.5 and 1. All alloys were solution annealed at 1200 °C for 100 h, then further aged at 600, 800 and 1000 °C for 1000 h. Characterisation was undertaken using a combination of X-ray diffraction (XRD), scanning and transmission electron microscopy (SEM and TEM), including electron back-scatter diffraction (EBSD), energy-dispersive X-ray spectroscopy (EDX) and selected area electron diffraction techniques. Mechanical properties were measured with microhardness. Results were compared to predictions made using Thermo-Calc software with the HEA4 database.

2. Experimental

Both experimental and modelling tests were conducted to test the thermal stability of the phases present in the $VCrMnFe Al_x$ alloy system. Thermo-Calc software (Thermocalc2020a) using the HEA4 database was used to predict the equilibrium phases present in the system. From [5] the HEA4 database was found to closely predict the phase formation in the similar TiVCrMnFe system. It was therefore deemed most appropriate to use in comparison to other databases available.

Five billets of $VCrMnFeAl_x$ were made by arc melting, with x = 0, 0.1, 0.25, 0.5 and 1.0. The alloys were cast using an Arcast 200 arc melter in an Ar atmosphere, with elemental metals of purity > 99.8% used. The billets were flipped 5 times and re-melted. They were homogenised at 1200 °C for 100 h, followed by water quenching. The

billets were then aged at 600, 800 and 1000 °C for 1000 h each. All ages were followed by a water quench.

SEM characterisation of the materials was conducted using a Zeiss Sigma with Oxford Instruments EDX and EBSD detectors. Samples were mechanically polished to a colloidal silica (50 nm) finish. EDX and EBSD maps were collected using a beam energy of 20 keV. All SEM-EDX maps were quantified in terms of wt% using Oxford Instruments' Aztec 4.0 software. Two phases were indexed in the EBSD maps; BCC and sigma. Note that the EBSD is not able to detect the difference between BCC (A2), B2 and Heusler phases. STEM spectrum imaging and TEM diffraction work was performed, using a 200 keV, X-FEG FEI Talos F200 S/TEM, to determine the exact phase structures. Mostly selected area diffraction patterns (SADPs) were used for this. However, in one instance ($VCrMnFeAl_{1.0}$ Aged at 800 °C) the volume of the phase was sufficiently small such that condensed beam electron diffraction (CBED) was used. Some interstitial based phases were observed in some of the alloys (e.g., vanadium carbides/nitrides/oxides) from impurities introduced during casting. Where present in the images, they are identified.

Microhardness measurements were made using a Matsuzawa MMT-X7A microindentor. A constant load of 1 kg was used with a 10 s dwell time, an average value of 20 measurements was reported.

3. Results

3.1. Alloy compositions

The alloy compositions as measured by large region (> 1.0 ×1.0 mm area) SEM-EDX scans are shown below in Table 1.

3.2. Sigma formation

After homogenisation at 1200°C, as well as after ageing at 1000°C, none of the alloys showed any evidence of sigma formation. After heat treatments at 600 and 800 °C, sigma phase was seen to form in $VCrMnFeAl_x$ for x = 0 and 0.1, but not at higher Al contents. Fig. 3 shows EBSD band contrast and phase maps for all the alloys. Note that the blue phase, indexed as BCC (A2), was not necessarily BCC (see Section 3.3), however EBSD cannot distinguish between BCC and BCC-based superlattice structures such as B2 and Heusler. Increasing the Al content from x = 0 to x = 0.1 significantly reduces the volume fraction of sigma phase formed at both 600 and 800 °C. At higher Al contents no sigma phase is formed at all. 800 °C produced a higher volume fraction of sigma phase than 600 °C in both the x = 0 and x = 0.1 alloys.

The phase compositions of the sigma and cubic phases in alloys VCrMnFe and $VCrMnFeAl_{0.1}$ are shown in Table 2. The compositions of both phases are very similar, with the exception of Al, which is present in much lower quantities in the sigma phase.

Table 1
Alloy compositions as measured by SEM-EDX in at% (standard deviation from 3 spectra).

x	Al	V	Cr	Mn	Fe
0		26.1 ± 0.2	25.6 ± 0.3	24.7 ± 0.3	23.6 ± 0.3
0.1	2.3 ± 0.2	26.9 ± 0.1	24.7 ± 0.1	21.9 ± 0.4	24.1 ± 0.2
0.25	6.6 ± 0.1	25.8 ± 0.1	23.5 ± 0.2	21.6 ± 0.1	22.5 ± 0.2
0.5	10.7 ± 1	24.3 ± 0.4	22.3 ± 0.3	20.8 ± 0.5	21.8 ± 0.7
1	20.8 ± 0.3	21.8 ± 0.2	20.2 ± 0.1	17.2 ± 0.1	19.9 ± 0.2

The precipitation of the sigma phase appeared to be very heterogeneous. With the possible exception of VCrMnFe aged at 800 °C, the sigma phase formed exclusively along grain boundaries and on interstitial (impurities including carbon and nitrogen) precipitate interfaces. Nucleation on interstitial-precipitate interfaces is shown in Fig. 4a-c, a low angle grain boundary can also be seen in Fig. 4d, along which, there is no obvious sigma phase.

3.3. Ordering due to Al addition

As well as suppressing sigma phase, TEM investigations revealed that increasing Al contents also drove ordering of the matrix.

3.3.1. Low Al (x = 0, 0.1)

After homogenisation at 1200°C, these alloys both appeared to be single-phase A2. With the exception of sigma phase (and interstitial precipitates), these alloys appeared to remain stable as a single A2 phase in all but one of their heat-treated conditions, see Fig. 5 and Fig. 6. The exception being $VCrMnFeAl_{0.1}$ which formed B2 in the matrix on aging at 600 °C.

3.3.2. Intermediate Al (x = 0.25, 0.5)

Both $VCrMnFeAl_{0.25}$ and $VCrMnFeAl_{0.5}$ appeared to be single phase after homogensiation at 1200 °C, see Fig. 7 and Fig. 8. The x = 0.25 alloy was A2 and x = 0.5 was B2 (although the presence of A2 could not be conclusively ruled out). After aging alloys with x = 0.25 and x = 0.5 at 600 °C, nano-segregation could be seen. In both alloys, Cr separates from Fe and Al. This segregation appeared to be much weaker in $VCrMnFeAl_{0.25}$, and the alloy appeared to be single phase B2. No diffraction spots from a Heusler phase was detected in this alloy, nevertheless, $VCrMnFeAl_{0.5}$ showed a Heusler diffraction pattern, and the segregation was more pronounced. Nano-segregation was not observed in either alloy at higher aging temperatures of 800°C and 1000°C. For all other aging temperatures $VCrMnFeAl_{0.25}$ appeared to be solely B2. $VCrMnFeAl_{0.5}$ appeared to be 100% Heusler at 800°C and 1000°C.

3.3.3. High Al (x = 1)

Fig. 9 shows the TEM results for the x = 1 alloy. Ignoring interstitial precipitates, the x = 1 alloy appeared to be single phase Heusler after homogenisation at 1200 °C and after ageing at 1000 °C. After aging at 800 °C, it showed a two-phase basket weave configuration. This is shown partially in Fig. 9, and on a larger scale in Fig. 12. One of the phases is Heusler (shown in the CBED diffraction pattern in Fig. 9). The second phase is less clear and is discussed below. The Heusler phase is comparatively enriched in V, Al and Fe.

This alloy differs from the rest in that at all heat treatments there is some nano-segregation occurring. This is most clear in the 600 °C aged condition, however, the other heat treatments show a 'mottling' effect in the spectrum images.

3.3.3.1. 600 °C. After aging at 600 °C, the microstructure of the x = 1 alloy became even more complex. Nano precipitates appear to have formed in the matrix, see Fig. 9. However, these precipitates are not present throughout the matrix. They do not form near grain boundaries or interstitial precipitates, this is illustrated in Fig. 10. They appear to be highly sensitive to the local vanadium concentration, which is depleted around the grain boundaries by the formation of carbides. The carbides preferentially nucleate along

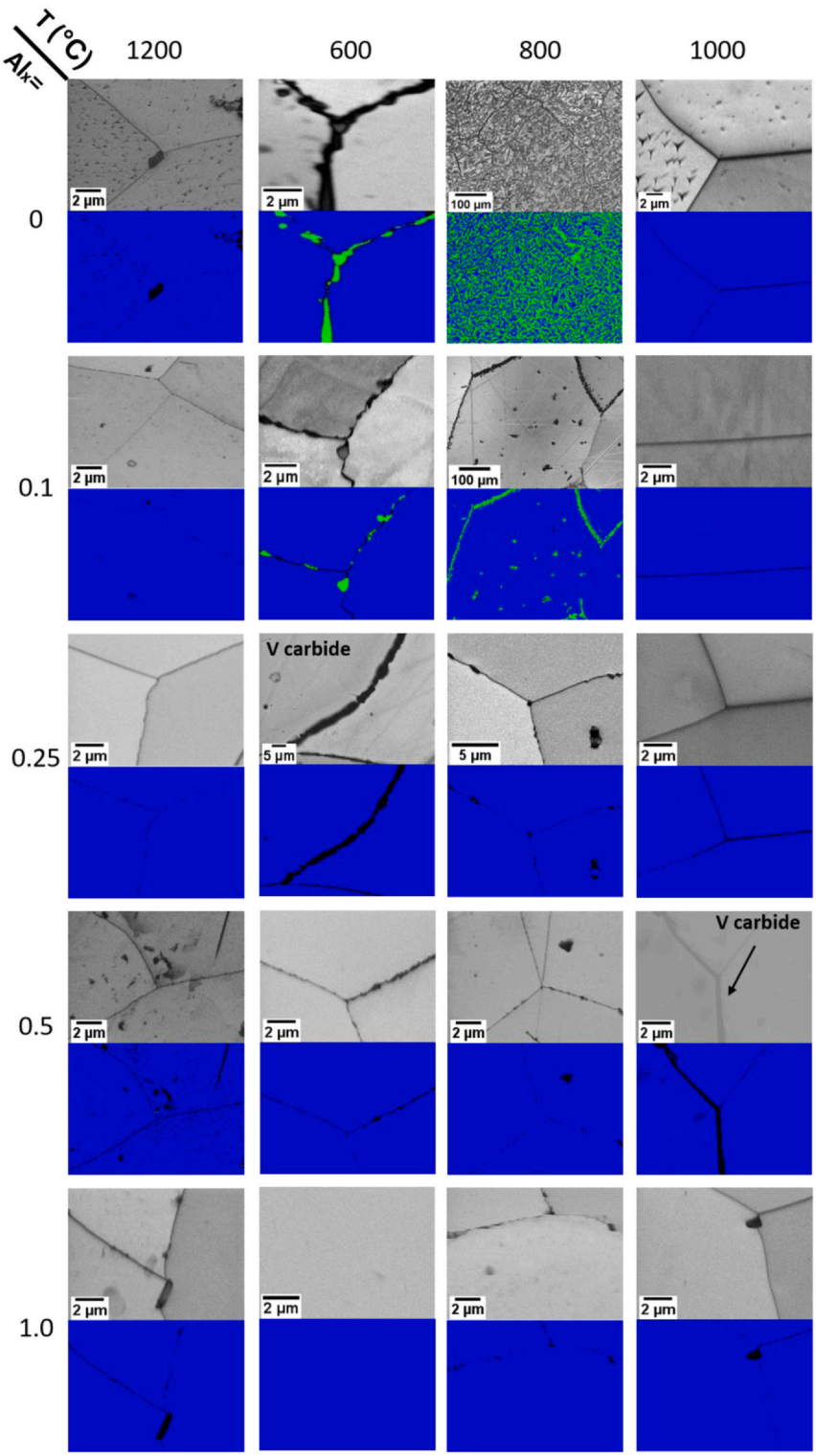

Fig. 3. SEM- EBSD band contrast and phase maps for $VCrMnFeAl_x$ alloys (where x = 0, 0.1, 0.25, 0.5 and 1.0) after being homogenised at 1200 °C and subsequently heat treated at 600, 800 and 1000 °C. In the phase maps blue was indexed as BCC (A2) and green was indexed as sigma.

Table 2
Phase compositions (at%) as calculated by SEM-EDX for $VCrMnFeAl_x$ after aging at 800 °C (standard deviation from spectra ± 0.1 at%).

x	Phase	Al	V	Cr	Mn	Fe
0	Sigma		25.8	22.3	24.9	27.0
	Cubic		28.90	30.7	21.9	18.5
0.1	Sigma	1.46	25.0	20.1	24.0	29.5
	Cubic	2.55	27.1	24.8	21.8	23.8

the grain boundaries, and hence the regions adjacent to the grain boundaries are generally depleted of vanadium. Furthermore, these nano precipitates appear to be coherent with the matrix. The matrix in the precipitate free region can be seen to be Heusler in Fig. 10, however no additional diffraction spots were observed in the precipitate containing region. Thus, the precipitates are most likely either another Heusler phase, or an A2 or B2 phase. Dark field imaging of these precipitates was inconclusive with regards to phase identification, see Supplementary Information.

Furthermore, similar to the intermediate Al content alloys (x = 0.25 and 0.5) aged at this temperature (600°C), the alloy also contained nano-segregation, see Fig. 11, which was taken in a precipitate free region adjacent to a vanadium carbide. As with the intermediate Al content alloys this is most clear in the separation of Cr from Fe. However, unlike those alloys, in this system, the Al does not follow the Fe segregation. Further to this, there are also minor V enrichments present. Overall, the microstructure formed by the alloy at 600 °C was complex.

3.3.3.2. 800 °C. Fig. 12 shows a larger field of view of $VCrMnFeAl_{1.0}$ aged at 800 °C, to illustrate the basket weave configuration of the two phases present within the alloy.

Two dark field images of the same sample are shown in Fig. 13, using electrons diffracted from a) a (111)-type Heusler reflection, and b) a (200)-type Hesuler reflection / (100)-type B2 reflection. The same regions appeared as dark stripes in both. Fig. 13b would therefore indicate that the Cr rich phase is A2, rather than B2. However, the CBED pattern taken from this region in Fig. 9 shows faint B2 spots. The relative intensities of these spots are shown in Fig. 13c. The intensity of the ordered reflections can be seen to be an order of magnitude lower in the Cr rich phase. It may be that, whilst the majority of the phase is A2, the 'mottling' is forming some short range ordering that, due to the thickness of the foil, even CBED is not able to fully differentiate between it and the A2.

Whilst it is therefore very difficult to differentiate between B2 and A2 in the case of the Cr rich, weakly diffracting with respect to Heusler planes, it is fair to conclude that it is more randomised than the neighbouring Heusler phase region.

The CBEDs in Fig. 9 also show that both phases have the same orientation (cube on cube orientation relationship). The weakly diffracting, Cr rich phase appears to have a preferred growth direction along < 110 > . Note, it is the Cr rich phase that has grown from

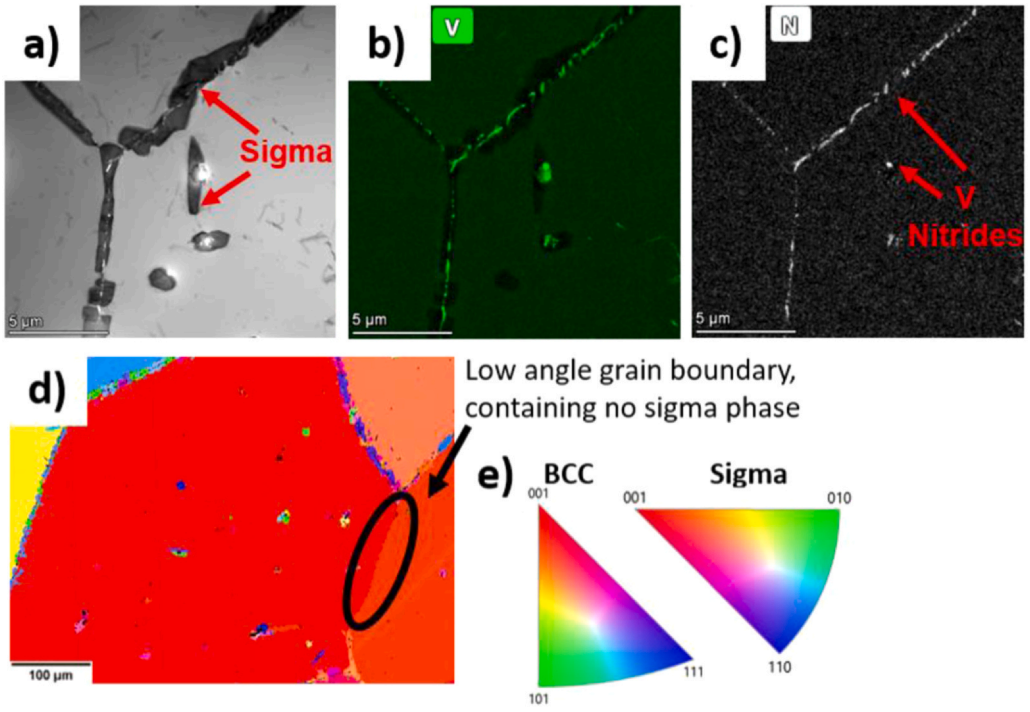

Fig. 4. a) STEM-BF and b-c) EDX elemental maps of VCrMnFe after aging at 600 °C for 1000 h. d) Inverse pole figure with respect to the z direction of the same region shown in Fig. 3 of alloy x = 0.1 heat treated at 800 °C. The orientation colour legend of which is shown in e). In both cases, sigma-phase has formed between grains and on vanadium nitrides, which are present due to N impurities, but not on the low angle grain boundary shown in d).

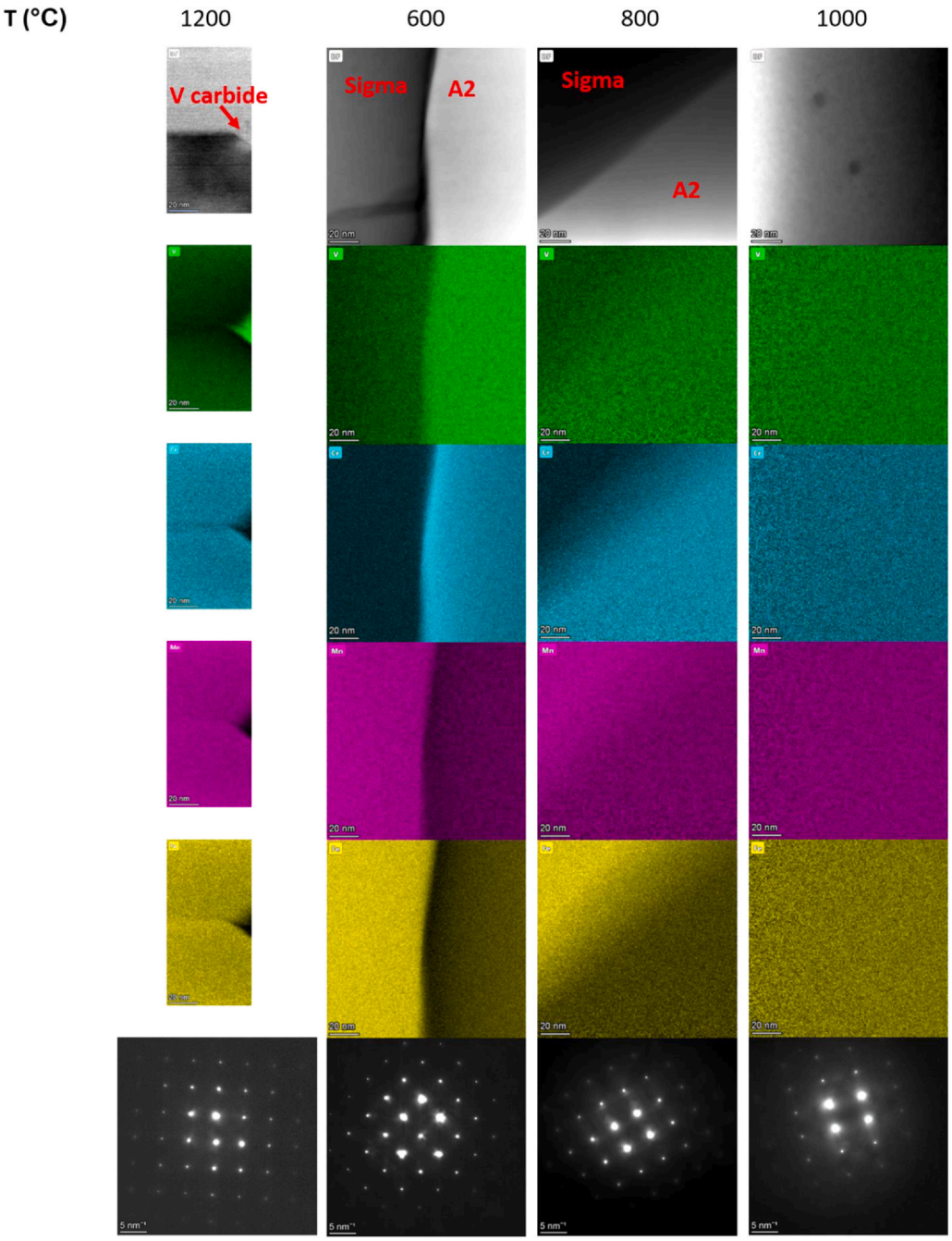

Fig. 5. STEM-BFs, EDX elemental maps and SADPs taken from VCrMnFe after solution annealing at 1200 °C and the three subsequent heat treatments. All SADPs are down the [100] zone axis of the matrix and show an A2 structure. The SADP after heat treatment at 1200 °C is reproduced from ref [5].

the Heusler phase, as the alloy was entirely Heusler phase after initially solution annealing at 1200 °C.

3.4. Mechanical properties

Microhardness measurements (20 per sample) were conducted on each alloy after each heat treatment. The results are shown, as a function of Al content, in Fig. 14.

With the exception of x = 0 and 0.1, there is little hardness variation for most of the alloys when comparing the results of the 800 °C,1000 °C and 1200°C (as-homogenised) heat treatments for each alloy. Comparing the different alloys, there is a slight hardening with increasing Al content in the homogenised (1200°C) states. This may be attributed to a slight increase in solid solution strengthening in the lower Al content alloys that are A2 at 1200 °C, and to ordering in the alloys with higher Al contents. An ordering effect on the

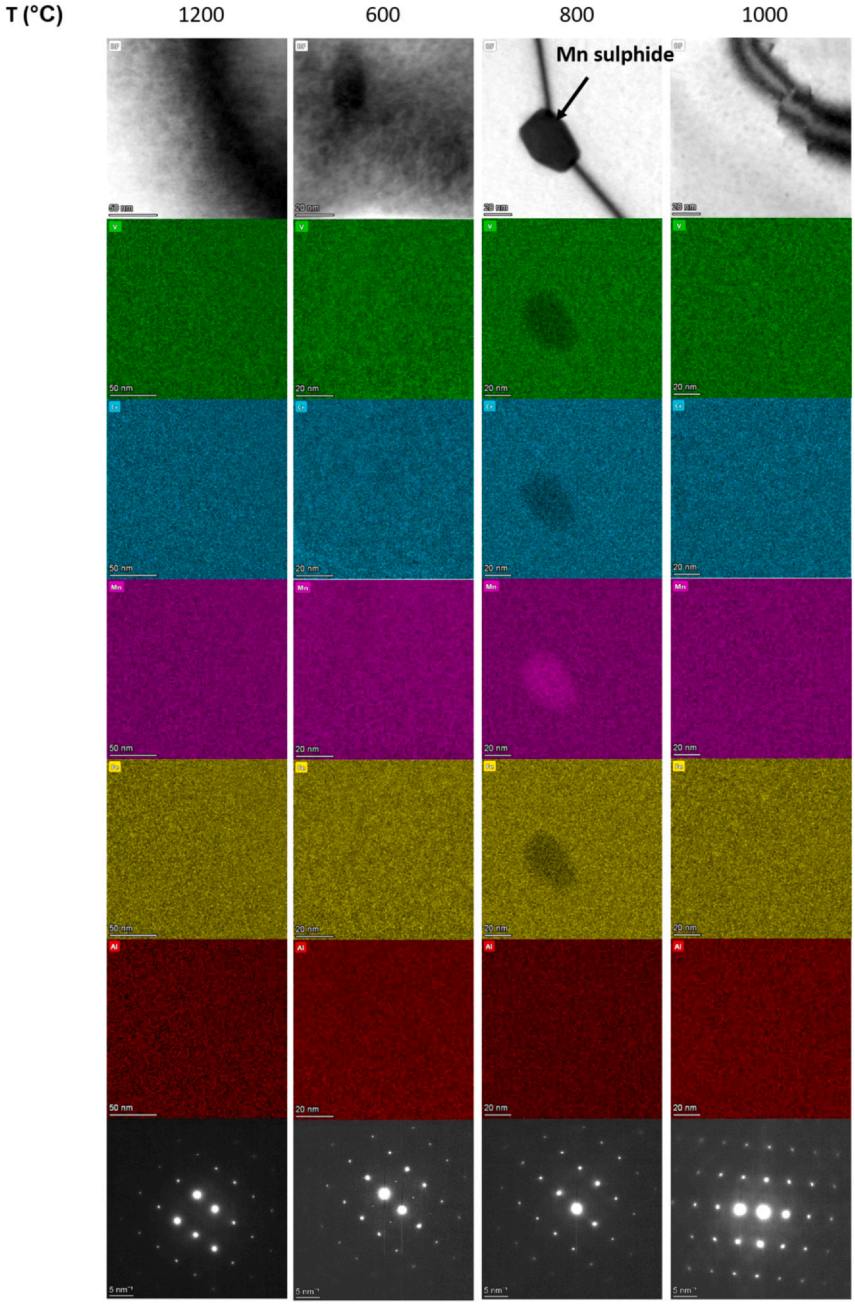

Fig. 6. a) STEM-BFs, EDX elemental maps and SADPs taken from $VCrMnFeAl_{0.1}$ after solution annealing at 1200 °C and the three subsequent heat treatments. All SADPs are down the [110] zone axis and show an A2 structure, with the exception of the alloy heat treated at 600 °C which is B2.

hardness may also be seen in $VCrMnFeAl_{0.5}$, which is softer in the B2 state (after annealing at 1200 °C) than the Heusler states (after aging at 800 and 1000 °C).

The alloys that have a significantly higher hardness are:

(i) Those containing sigma phase. This is consistent with the high hardness of sigma phases. VCrMnFe aged at 800 °C, had by far the most sigma phase present and can be seen to be by far the hardest material.

(ii) $VCrMnFeAl_{0.25}$, $VCrMnFeAl_{0.5}$ and $VCrMnFeAl_{1.0}$ after aging at 600 °C. These alloys have nanoscale (< 10 nm) separation of Cr and Fe.

3.5. Thermo-Calc Predictions

Thermocalc predictions for this alloy system are shown in Fig. 15.

From Fig. 15, it is evident that VCrMnFe is predicted to be a single phase BCC solid solution at 1200 °C, and begins to form sigma below

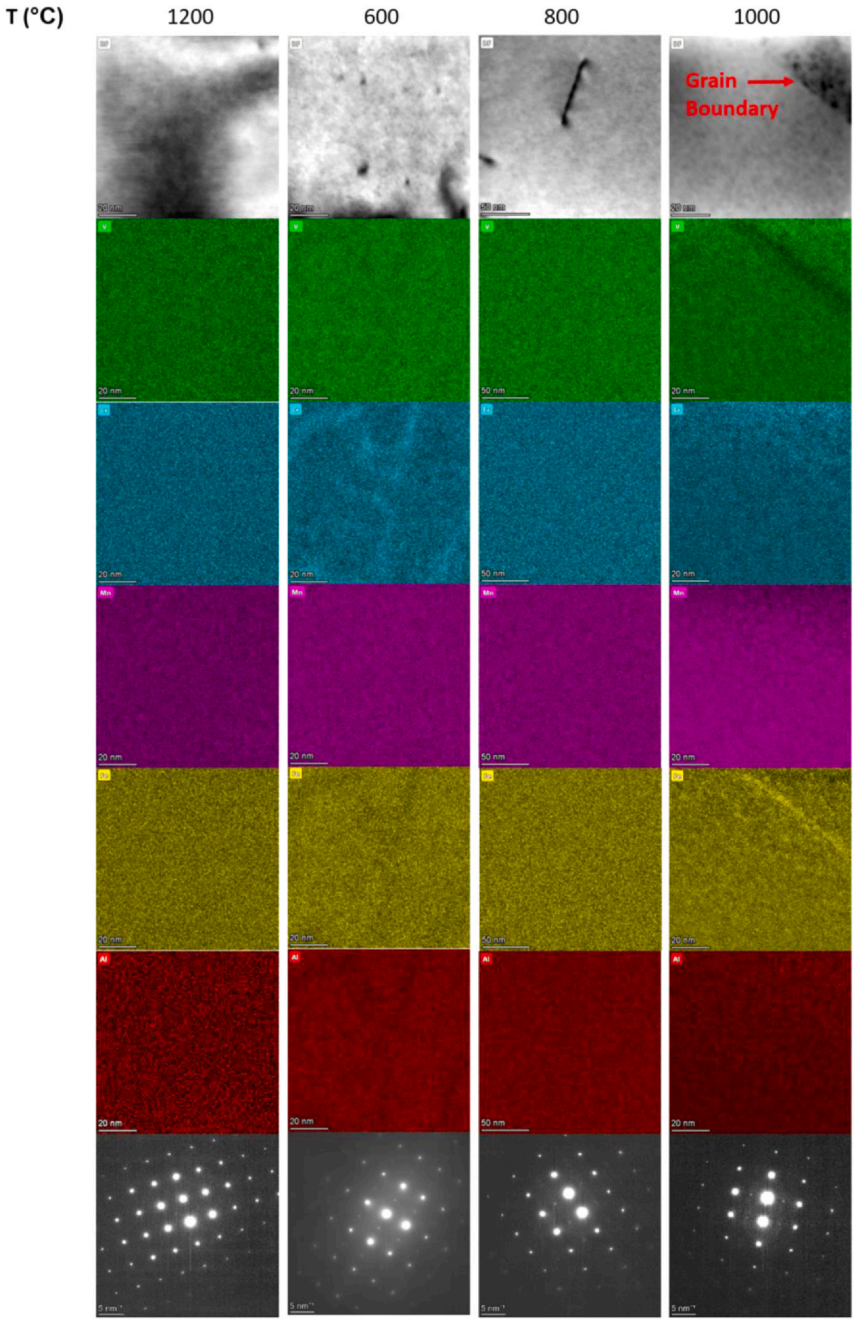

Fig. 7. STEM-BFs, EDX elemental maps and SADPs taken from $VCrMnFeAl_{0.25}$ solution annealing at 1200 °C and the three subsequent heat treatments. The SADP from the heat treatment at 1200 heat treatment is down the [100] zone axis and shows an A2 structure. SADPs from heat treatments at 600 – 1000 °C are down the [110] zone axis and show a B2 structure. Nano-segregation can be seen after heat treatment at 600 °C.

1000°C. This is in agreement with the trends shown in Fig. 3. Two sigma phases are predicted to form the compositions of which are shown in Table 3. Sigma #1 is richer in Mn and poorer in V, and vice versa for sigma #2. Neither sigma #1 nor sigma #2 fully match the observed composition of the sigma phase, which contained significant quantities of both V and Mn (see Table 2). Increasing the Al content is predicted to reduce the stability of both of these sigma phases. This is broadly in agreement with the experimental results, however, the sigma #2 phase is predicted to be stable at much higher Al contents than were observed experimentally. The Sigma phase was predicted to have essentially zero solubility of Al, however, this too was not the case experimentally; Table 2 shows the sigma phase to contain ~1.5 at% Al in $VCrMnFeAl_{0.1}$.

Increasing the Al content was also predicted to stabilise the B2 phase. However, again, less so than was experimentally observed. According to Thermo-Calc, no B2 should have been observed in $VCrMnFeAl_{0.1}$ and should only have been found after aging at 600 °C in $VCrMnFeAl_{0.25}$ and $VCrMnFeAl_{0.5}$.

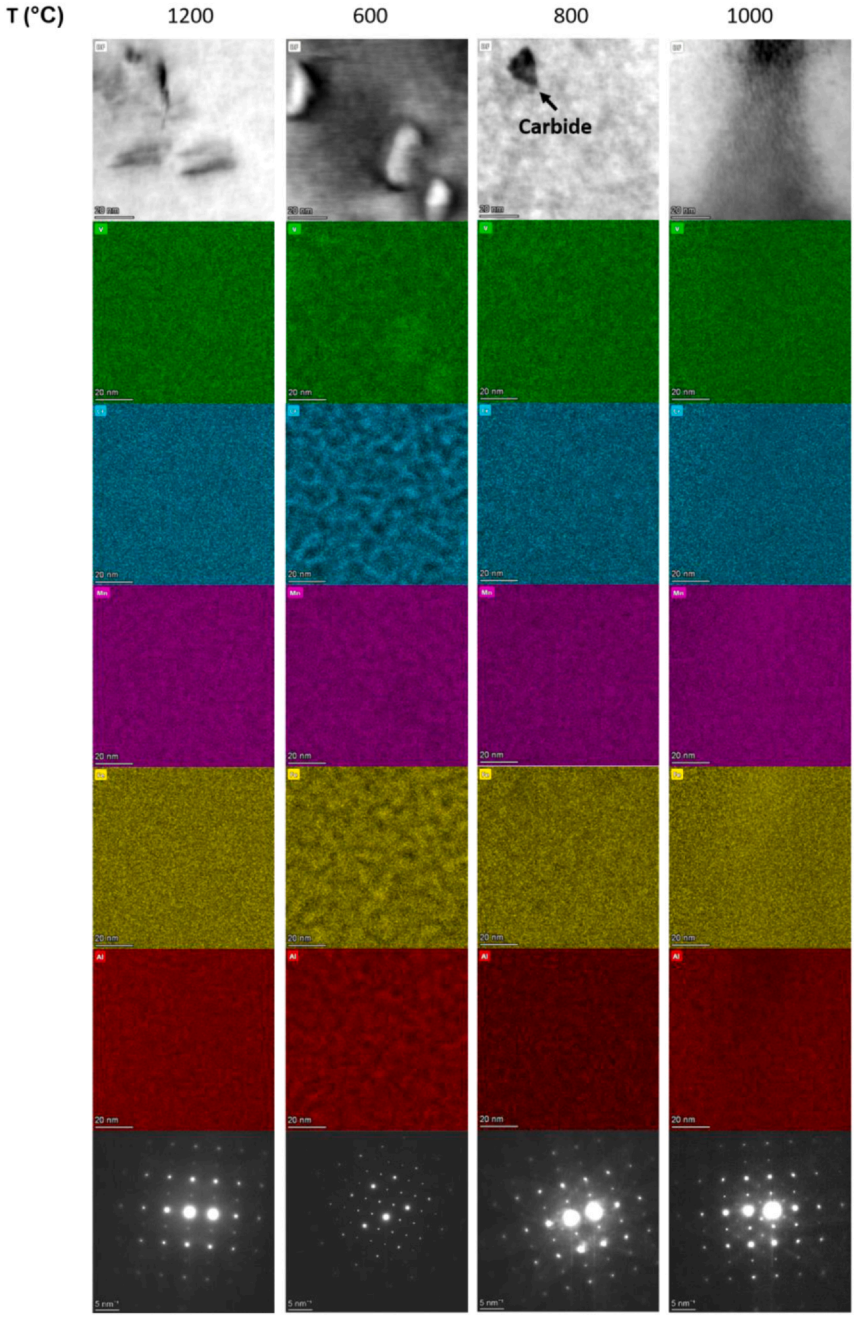

Fig. 8. STEM-BFs, EDX elemental maps and SADPs taken from $VCrMnFeAl_{0.5}$ after solution annealing at 1200 °C and the three subsequent heat treatments. All SADPs are down the [110] zone axis. B2 is present in the solution annealed (at 1200 °C) condition and Heusler structures are present after heat treatments at 600 – 1000 °C, and. Nano-segregation can be seen after heat treatment at 600 °C.

4. Discussion

4.1. Sigma Phase

Sigma phase was only observed in a limited number of alloys/heat treatments. No sigma phase was observed in any heat-treated state of the alloys where $x \geq 0.25$. In the alloys that sigma phase formed in, the optimal temperature for producing the largest volume fraction is between 600 and 1000 °C, with 800 °C being found to lead to the largest volume fractions forming.

Given this, it would appear that the minimum Al content to stop sigma phase precipitation is between 2.3 and 6.6 at%. It is likely that this minimum Al content is nearer 2.3 than 6.6 at%, given the significant phase proportion reduction between $x = 0$ and $x = 0.1$. From Fig. 3, sigma phase proportions of 55% and 4% were measured respectively.

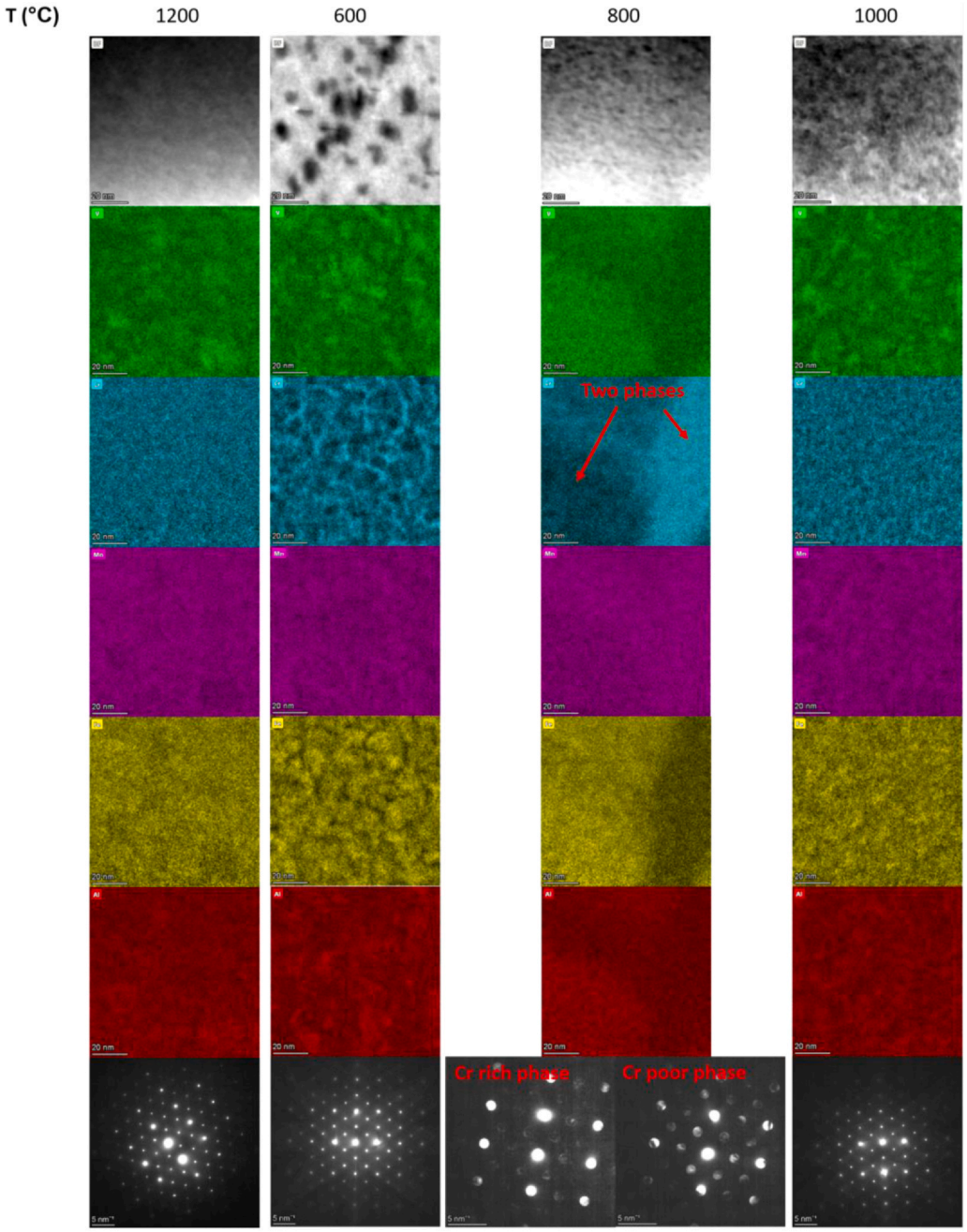

Fig. 9. STEM-BFs, EDX elemental maps and diffraction patterns taken from $VCrMnFeAl_{1.0}$ after solution annealing at 1200 °C and the three subsequent heat treatments. All diffraction patterns are down the [110] zone axis and show a Heusler structure, with the exception of the Cr rich phase after aging at 800 °C, which shows a phase with the Heusler planes diffracting more weakly. Note the diffraction patterns taken at 800 °C are CBEDs due to the small size of the two phases.

Fig. 4 also demonstrates that another avenue for reducing sigma phase formation would be careful grain boundary engineering and interstitial content control.

4.1.1. Composition

From Table 2, the compositions of the BCC and sigma phases are very similar. Modifying the compositions of the alloys with respect to V, Cr, Mn and Fe may therefore have relatively little effect, especially when compared with the effects of small additions of Al. For instance, the work of Barron et al. [16], showed that sigma phase does not form when Fe is absent from the system (VCrMn). This is corroborated by Thermo-Calc prediction in Fig. 16. Note from Table 2, Fe is enriched to a greater extent than Mn is in the sigma phase. However, this alloy is different by 25 at% Fe, rather than 6.6 at% Al.

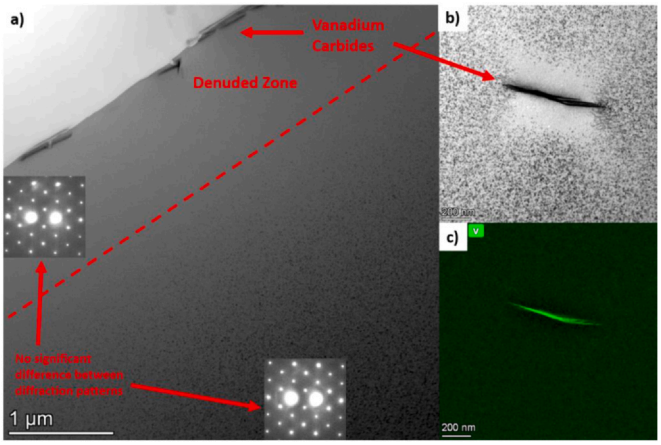

Fig. 10. STEM analysis of $VCrMnFeAl_{1.0}$ aged at 600 ºC. a) STEM-BF showing precipitate denuded zone adjacent to a grain boundary containing vanadium carbides. Both the precipitate containing and denuded zones show a Heusler diffraction pattern. b) STEM-BF showing a similar denuded zone around a vanadium carbide with c) the corresponding vanadium map showing vanadium depletion in the precipitate denuded zone.

This validates the decision to modify the phases with additional elements, rather than modifying the proportions of the other elements already present.

4.1.2. Comparison with thermo-calc

For x = 0, there is a very good agreement between the HEA4 database and the experimentally observed phases. No sigma-phase was observed at 1000 °C and after aging at 800 °C for 1000 h, a sigma-phase fraction of 55% was found, compared with a phase fraction of 50% predicted by HEA4 at this temperature. There is poorer agreement at 600 °C. However, it could be argued that the alloy system is most likely not in equilibrium, due to insufficient kinetics at this temperature for the redistributions required.

Once Al is added, the HEA4 database appears to be less reliable. For x = 0.1, the HEA4 database predicts the slightly lower start temperature of 900 °C for the onset of sigma-phase formation, however, at 800 °C it still predicts 30% sigma-phase, far more than was observed. Further to this, it predicts that 15 at% Al should be required to stop sigma phase forming at 600 °C, far more than the observed 6.6 at%. Furthermore, it fails to predict any Heusler phase in any of the alloys investigated.

4.1.3. Predicting sigma phase using parametric approaches

Both the valence electron concentration (VEC) and the proportion of sigma forming elements in HEAs have been linked to whether or not sigma phase will form [17,18]. It has been reported that for sigma phase to form in HEAs, the VEC of an alloy needs to lie within a range of values; 6.88–7.84 and the proportion of sigma forming elements must be sufficiently high. However, the alloys investigated here do not conform to this trend. By the definition of ref. [18], the proportion of sigma forming elements is 100% in VCrMnFe, but the VEC is 6.5. The small additions of Al necessary to stop the formation of sigma phase (e.g., in $VCrMnFeAl_{0.25}$) has relatively little effect on both these parameters (VEC=6.3 and proportion of sigma forming elements = 93%). In these HEAs at least, there must therefore be more determining the formation or not of sigma phase than captured by these simple measures.

4.2. Ordering

Increasing the Al content of these alloys and/or lowering the aging temperature was found to increase the stability of ordered phases, with the preference moving from A2 to B2 to Heusler. The results from Section 3.3 are summarised in Fig. 17.

That $VCrMnFeAl_{0.1}$ and $VCrMnFeAl_{0.25}$ form a B2 phase at all, is an interesting result. The $Fe_{1-2y}V_yAl_y$ system exhibits a similar array of phases, namely, A2, B2 and Heusler, dependent upon the value of y and the heat treatment [19–21]. Interestingly, the $Fe_{1-2y}V_yAl_y$ system appears to have a much higher tolerance for Al content in the A2 phase, even at temperatures as low as 600 °C. It can therefore be inferred that the additions of Cr and Mn (at the expense of Fe) necessary to form the alloys examined in this system reduce the solubility of Al in the alloy system. This cannot be attributed to a lower solubility of Al in Cr or Mn, as both elements [22,23] have significantly higher solubility of Al than seen in this study. This is contrary to the notion that high entropy alloys have increased single-phase stability.

Indeed, further evidence of reduced solubility of Al in higher entropy alloys within the VCrMnFeAl system can be seen by

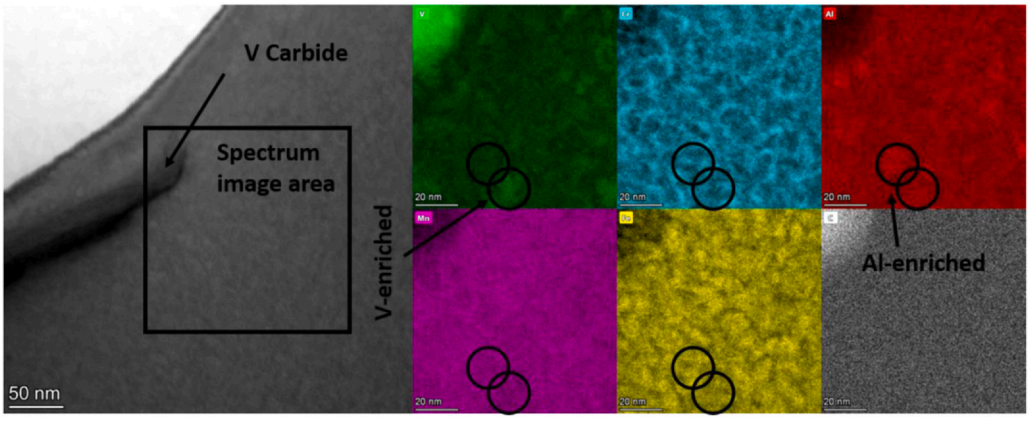

Fig. 11. STEM-BF and EDX elemental maps of $VCrMnFeAl_{1.0}$ aged at 600 °C for 1000 hrs. Two regions are circled showing slight vanadium and aluminium enrichments respectively, which do not appear to correlate strongly with any other elemental segregation.

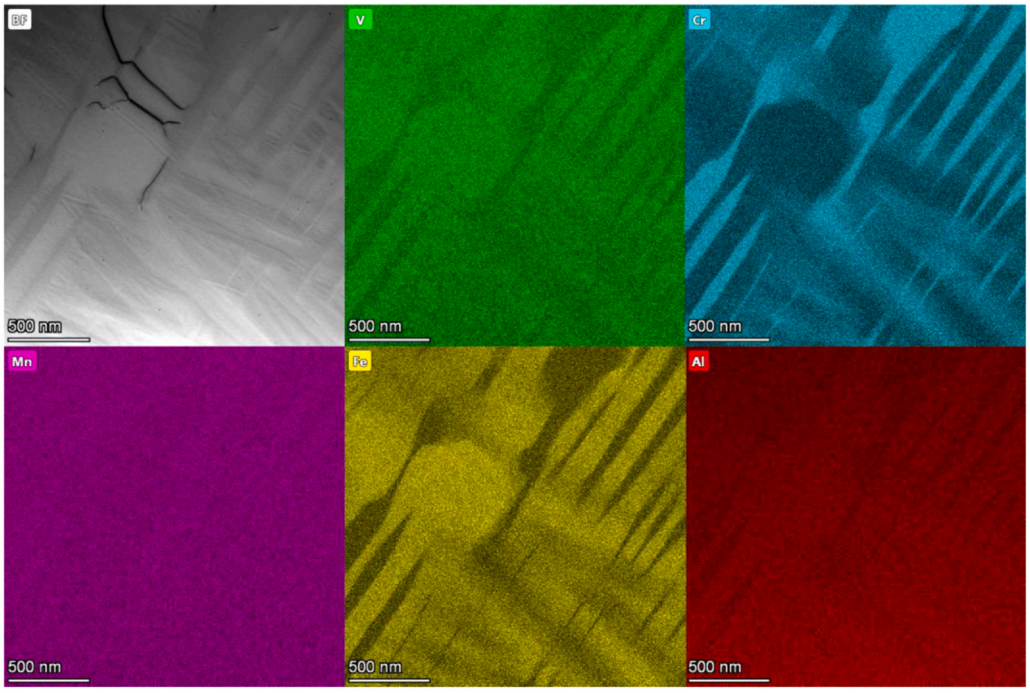

Fig. 12. STEM-BF and EDX elemental maps of VCrMnFeAl aged at 800 °C for 1000 hrs. The region is viewed down the [110] zone axis and shows a basket-weave microstructure.

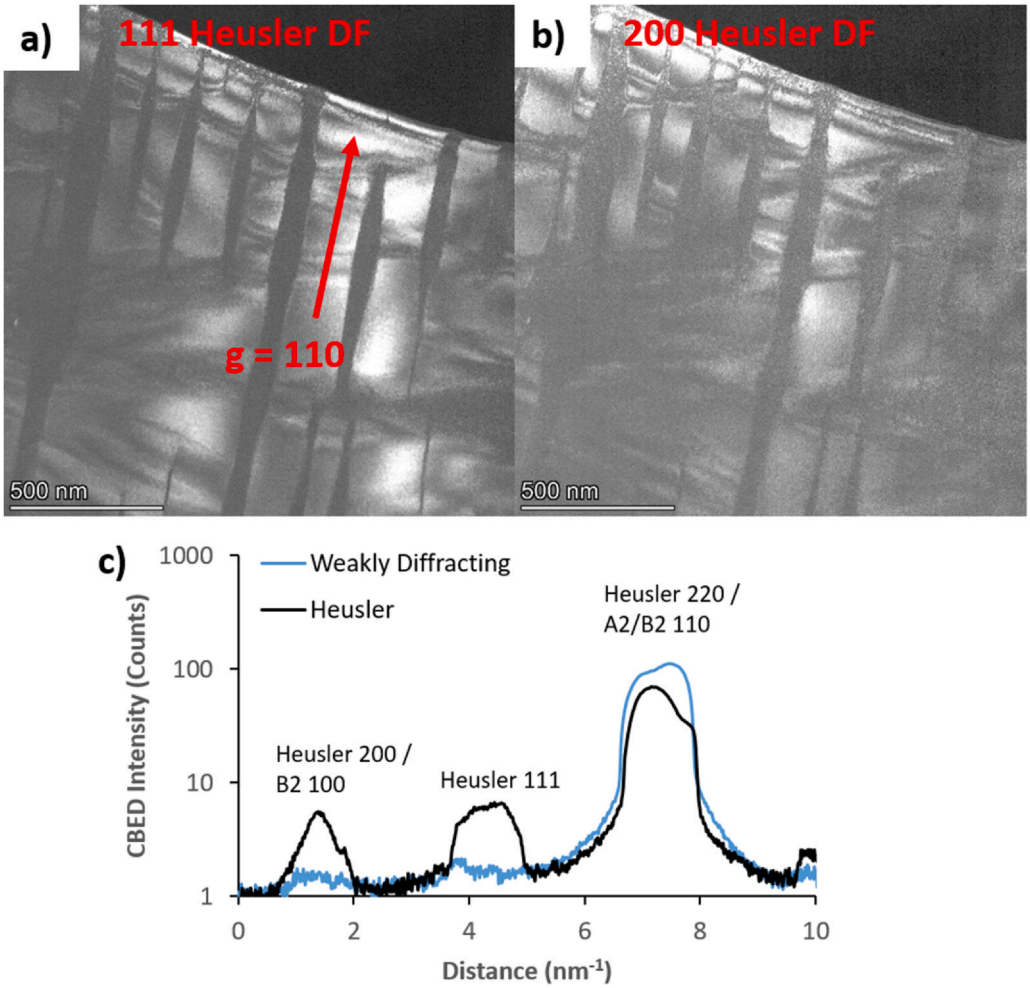

Fig. 13. TEM-DFs of VCrMnFeAl aged at 800 °C for 1000 hrs created from the a) (111) and b) (200) Hesuler spots. C) shows the relative intensities of the CBED spots of the two phases.

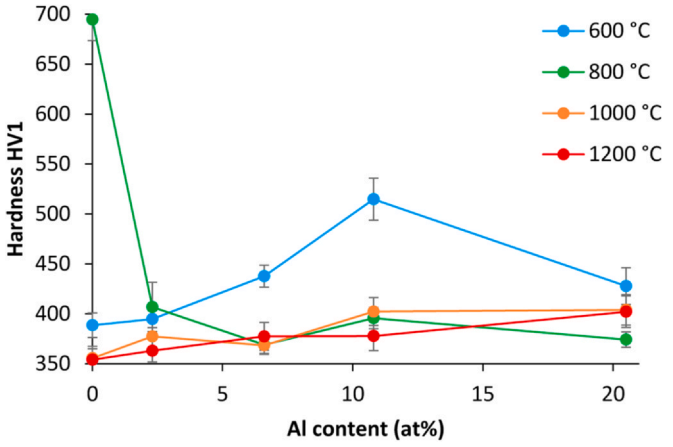

Fig. 14. Microhardness of $VCrMnFeAl_x$ after solution annealing at 1200 °C for 100 h and aging at 600, 800 and 1000 °C for 1000 h. The error bars are the standard deviation of 20 measurements. The lines between the points are included only to guide the eye and should not be taken to show precise trends.

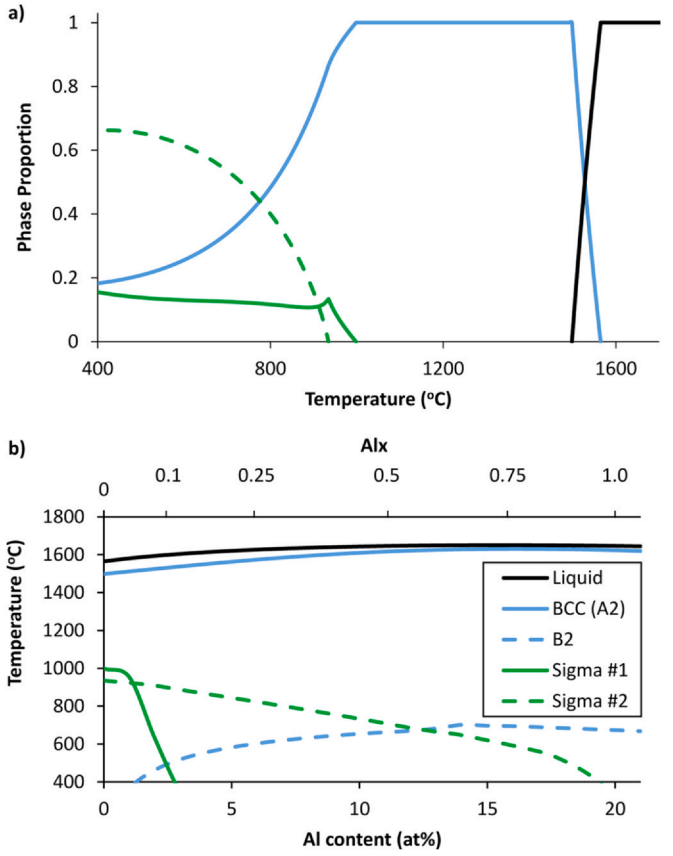

Fig. 15. Themocalc predictions using the HEA4 database for equi-atomic VCrMnFe a) phase proportions as a function of temperature and b) as a function of Al content (all other elements being equal).

comparing $VCrMnFeAl_{0.5}$ with $VCrMnFeAl_{1.0}$ aged at 800 °C. The lower Al content, $VCrMnFeAl_{0.5}$ alloy, was composed of a majority, if not single, Heusler phase, whereas $VCrMnFeAl_{1.0}$ contained a second,

Table 3
Compositions of sigma phase at 800 °C, in at%, for the alloy compositions listed in Table 1 as predicted by Thermo-Calcs HEA4 database. Sigma #2 is not predicted to form at 800 °C in $VCrMnFeAl_{0.1}$.

Alloy	Phase	Al	V	Cr	Mn	Fe
VCrMnFe	Sigma #1		15.7	25.6	28.3	30.1
	Sigma #2		33.0	22.4	8.3	36.3
$VCrMnFeAl_{0.1}$	Sigma #1	0.02	18.0	26.5	23.3	32.2

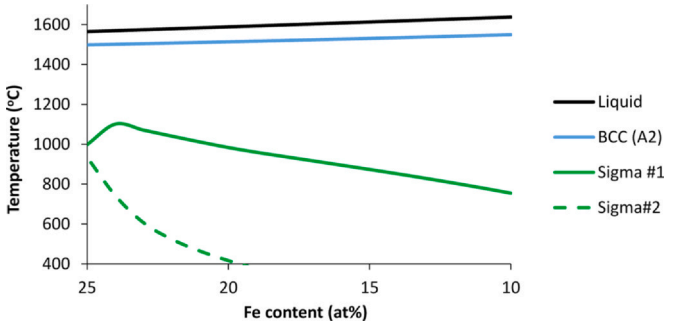

Fig. 16. Themocalc predicted phase diagram using the HEA4 database for VCrMnFe as a function of Fe content.

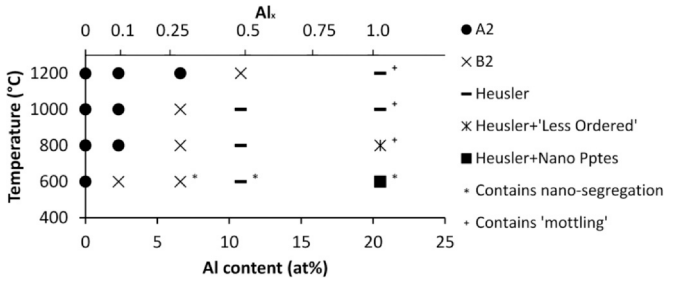

Fig. 17. Majority matrix phases present (not including sigma or interstitial phases) in $VCrMnFeAl_x$ as a function of aging temperature. It should be noted that it was not possible to conclusively rule out the existence of some phases in the presence of others, e.g., small quantities of B2 in a majority Huesler structure.

weakly diffracting, phase, that was at least more randomised than Hesuler phases. This weakly diffracting phase, however contained a high Al concentration than the solid Heusler phase seen in $VCrMnFeAl_{0.5}$. A major difference between these two phases then, is a lower entropy in the weakly diffracting phase due to segregation of the other four elements.

It is difficult to categorically determine in this study whether or not the nano-segregation observed was two separate crystal structures or not. The segregation was sufficiently small, such that even CBED would not have been sufficient to conclude on this. The foil would have been sufficiently thick such that both Heusler and non-Heusler regions could have interacted with the beam. However, examining $VCrMnFeAl_{0.5}$ aged at 600 °C; Fig. 18 shows both the segregation in this alloy with a dark field image collected using electrons diffracted from the (111) Heusler plane. No great correlation between the brightly imaging regions and the Cr depletion can be seen. It should also be noted that the Cr appears to segregate over length scales greater than the brightly imaging spots.

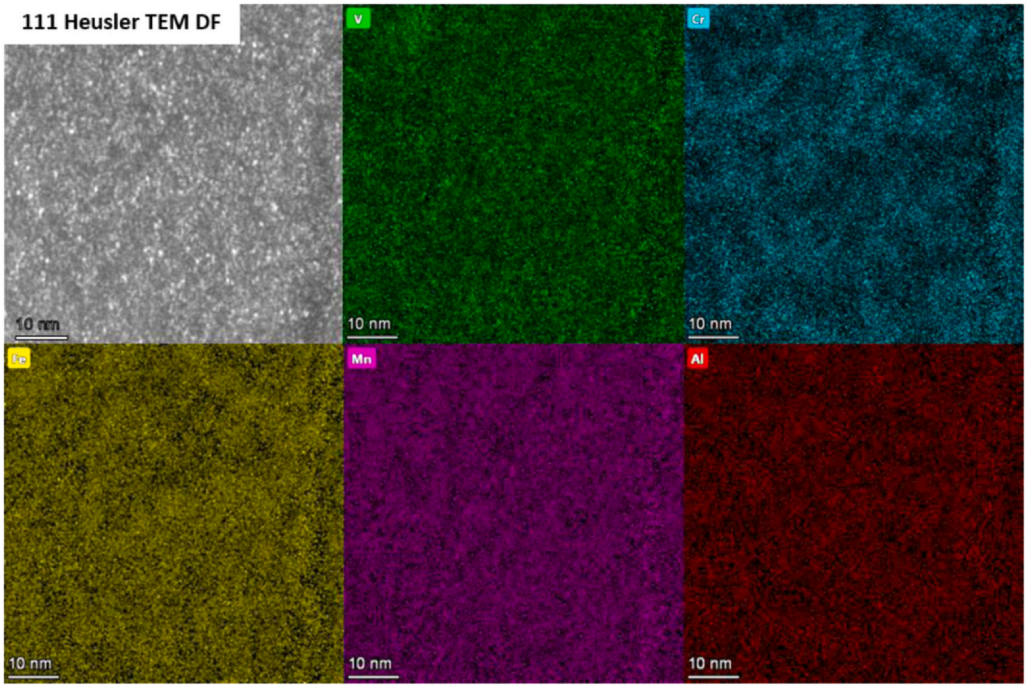

Fig. 18. TEM-DF taken from the (111) Heusler reflection and STEM-EDX spectrum images from $VCrMnFeAl_{0.5}$ aged at 600 °C. There is no significant correlation between the segregation and the brightly imaging regions in the DF image.

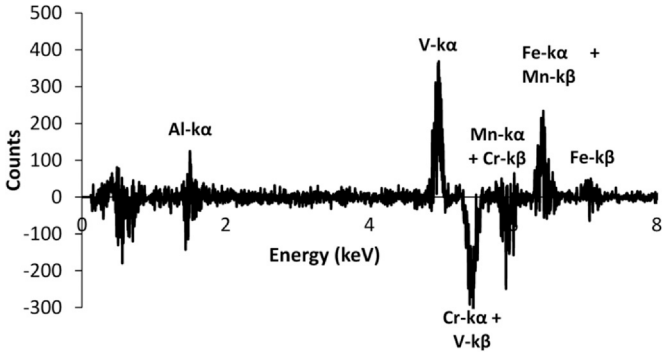

Fig. 19. The difference in EDX spectra between the matrix and the precipitates in $VCrMnFeAl_{1.0}$ aged at 600 °C for 1000 h.

The nano-segregation observed also made quantifying the elemental distributions across the nano precipitates in $VCrMnFeAl_{1.0}$ after aging at 600 °C non-trivial. Fig. 19 shows a spectrum produced by subtracting spectra from the matrix from spectra from the precipitate regions in the EDX map taken in Fig. 9. Thus, positive peaks indicate an enrichment in the precipitates and negative peaks indicate a depletion, relative to the matrix. The precipitates can be seen to be depleted, relative to the matrix, in Cr and enriched in Fe and V, which is to be expected given they do not form in vanadium depleted regions. Crucially, there is very little Al segregation between the precipitates and the matrix. As the Al content has been shown to be strongly associated with the ordering of these alloys, it may be that these precipitates are, like the matrix, also Heusler. However, this is not definitive. This can be seen as an extension of the nano-segregation seen in the precipitate free regions. There is sufficient Al for both segregated regions to be Heusler, but the alloy separates into a V and Fe enriched, and a Cr enriched phase. In the region containing reduced V concentrations, the alloy is segregated, but no second phases were detected. But at higher V concentrations, a separate phase is formed.

4.2.1. Stoichiometric considerations

There are three sites in the Heusler $L2_1$ structure: X, Y and Z, with the structure taking the form of X_2YZ. As was stated in the introduction, within the element combinations examined in this study, the previously found possible Heusler phases that could form are: Fe_2VAl, Mn_2VAl and Fe_2CrAl [13]. Note that Mn_2CrAl has not been observed in the literature. It can be seen that in the aforementioned stoichiometric $L2_1$ structures, Fe and Mn occupy the X site, V and Cr occupy the Y site and Al occupies the Z site.

The results show (e.g. Figs. 7–9) a separation of Cr from Fe and Al in the higher Al content alloys (where more ordering is present). This can be explained as follows. There is too little Fe+Mn to occupy the X site, and too much V+Cr to occupy the Y site. Given that Mn_2CrAl has not been reported as a phase, it is unlikely that Mn and Cr are stable together. From a stoichiometric consideration, in this alloy system, uptake of Mn and Fe is more preferential in the Heusler phase than Cr. The Cr was not found to be zero in any regions, however. Thus Fe likely segregated to these regions more strongly than Mn as it was more stable in the non-zero Cr regions.

4.3. Hardening

Nano-segregation can be seen to increase the hardness of these alloys. It appears that to have a significant effect, however, the segregation must be extremely fine, on length scales < 10 nm. Even plates with widths on the order of 10–100 nm seen in $VCrMnFeAl_{1.0}$ after aging at 800 °C were insufficiently small to produce significant

hardness increases. Rather, this alloy is softer than in this condition than it is after aging at 1000 and 1200 °C due to the presence of the softer, weakly diffracting phase. Comparing these results with the VCrMn system[16], Fe can be seen to have a slight softening effect on the alloy system (in the solution annealed state).

With regards to other mechanical properties, whilst no quantified assessments were made, it was noted in the course of experimentation that the higher the Al content of the material, the more brittle and difficult it was to process. The x = 0.5 and 1.0 alloys regularly cracked and snapped during cutting and mechanical thinning.

5. Conclusions

- All alloys examined in the $VCrMnFeAl_x$ system formed a matrix phase based on the BCC structure.
- Sigma phase was found to form in low Al containing alloys (2.3 and 0 at% Al) after aging at temperatures below 1000 °C, with the largest proportion of sigma-phase occurring after aging at 800 °C.
- Small additions of Al significantly inhibited the stability of sigma phase in the VCrMnFe system. 6.6 at% Al was sufficient to stop any sigma-phase forming after all heat treatments (after 1200°C homogenisation and subsequent ageing at 600°C, 800°C or 1000°C for 1000 h).
- Higher Al contents were found to cause an ordering of the cubic phase, with progressively higher levels leading to a change from BCC (A2) to B2 to Heusler. B2 and Heusler phases were found after additions of 2.3 and 10.7 at% Al respectively.
- Whilst the HEA4 database was found to be good at predicting the phases present in the x = 0 system and predicts that Al additions would reduce the sigma phase, it significantly overestimated the Al content needed and failed to predict the presence of Heusler phase.
- The higher Al content alloys presented several very interesting and complex microstructures. After aging $VCrMnFeAl_{1.0}$ at 600 °C, coherent nano-precipitates amidst nano-segregation that were highly sensitive to V concentrations formed. After aging $VCrMnFeAl_{1.0}$ at 800 °C, a two-phase coherent, cube-on-cube orientated, basket weave microstructure formed.

CRediT authorship contribution statement

A.W. Carruthers: Conceptualisation, Methodology, Software, Formal analysis, Investigation, Writing – original draft. **H. Shahmir:** Validation, Methodology, Resources, Writing – review & editing. **L. Hardwick:** Software. **R. Goodall:** Software. **A.S. Gandy:** Resources, Writing – review & editing, Project administration, Funding acquisition. **E.J. Pickering:** Conceptualisation, Validation, Writing – review & editing, Supervision, Project administration, Funding acquisition.

Declaration of Competing Interest

The authors declare that they have no known competing financial interests or personal relationships that could have appeared to influence the work reported in this paper.

Acknowledgement

This work was funded through EPSRC grants EP/R021864/1 and EP/R021546/1. We also wish to acknowledge the support of the Henry Royce Institute for Advanced Materials for E.J. Pickering's time, as well as access to the FEI Talos electron microscope at Royce@Manchester, funded through EPSRC grants EP/R00661X/1, EP/S019367/1, EP/P025021/1 and EP/P025498/1. The raw data associated with this work can be accessed via the following link: https://zenodo.org/record/4633926#. YFxZgq_7SUk DOI: 10.5281/zenodo.4633926.

Appendix A. Supporting information

Supplementary data associated with this article can be found in the online version at doi:10.1016/j.jallcom.2021.161525.

References

[1] E.J. Pickering, A.W. Carruthers, P.J. Barron, S.C. Middleburgh, D.E.J. Armstrong, A.S. Gandy, High-entropy alloys for advanced nuclear applications, Entropy 23 (98) (2021) 1–28.
[2] M. Fleming, J.C. Sublet, M. Gilbert, High-energy activation simulation coupling TENDL and SPACS with FISPACT-II, J. Phys.: Conf. Ser. 1046 (2018) 012002, https://doi.org/10.1088/1742-6596/1046/1/012002
[3] M.R. Gilbert, M. Fleming, and J.-C. Sublet, Automated Inventory and Material Science Scoping Calculations under Fission and Fusion Conditions, 2017.
[4] M.R. Gilbert, T. Eade, T. Rey, R. Vale, C. Bachmann, U. Fischer, N.P. Taylor, Waste implications from minor impurities in European DEMO materials, Nucl. Fusion 59 (2019) 076015, https://doi.org/10.1088/1741-4326/ab154e
[5] A.W. Carruthers, B.S. Li, M. Rigby, L.C. Raquet, R. Mythili, C. Ghosh, A. Dasgupta, D. Armstrong, A.S. Gandy, E.J. Pickering, Novel reduced-activation TiVCrFe based high entropy alloys, J. Alloy. Compd. 856 (2021) 157399, https://doi.org/10.1016/j.jallcom.2020.157399
[6] S.S. Mishra, T.P. Yadav, O.N. Srivastava, N.K. Mukhopadhyay, K. Biswas, Formation and stability of C14 type Laves phase in multi component high-entropy alloys, J. Alloy. Compd. 832 (2020) 153764, https://doi.org/10.1016/j.jallcom.2020.153764
[7] T.P. Yadav, S. Mukhopadhyay, S.S. Mishra, N.K. Mukhopadhyay, O.N. Srivastava, Synthesis of a single phase of high-entropy Laves intermetallics in the Ti–Zr–V–Cr–Ni equiatomic alloy, Philos. Mag. Lett. 97 (12) (2017) 494–503, https://doi.org/10.1080/09500839.2017.1418539
[8] T.B. Massaiski, J.L. Murray, L.H. Bennet, H. Baker, Binary Alloy Phase Diagrams Vols 1 and 2, American Society for Metals,, Ohio, 1986.
[9] G. Ghosh and M. Materials Science International Team, Partial isothermal section at 750°C: Datasheet from MSI Eureka in SpringerMaterials (⟨https://materials.springer.com/msi/phase-diagram/docs/sm_msi_r_10_014873_01_full_LnkDia5⟩). MSI, Materials Science International Services GmbH, Stuttgart, Available at: ⟨https://materials.springer.com/msi/phase-diagram/docs/sm_msi_r_10_014873_01_full_LnkDia5⟩.
[10] P. Villars and H. Okamoto, Eds., Al-Fe-V Isothermal Section of Ternary Phase Diagram: Datasheet from 'PAULING FILE Multinaries Edition – 2012′ in SpringerMaterials (⟨https://materials.springer.com/isp/phase-diagram/docs/c_1100132⟩). Springer-Verlag Berlin Heidelberg & Material Phases Data System (MPDS), Switzerland & National Institute for Materials Science (NIMS), Japan, [Online]. Available: ⟨https://materials.springer.com/isp/phase-diagram/docs/c_1100132⟩.
[11] P. Villars and H. Okamoto, Eds., Cr-Fe-Ga Isothermal Section of Ternary Phase Diagram: Datasheet from 'PAULING FILE Multinaries Edition – 2012′ in SpringerMaterials (⟨https://materials.springer.com/isp/phase-diagram/docs/c_2000114⟩). Springer-Verlag Berlin Heidelberg & Material Phases Data System (MPDS), Switzerland & National Institute for Materials Science (NIMS), Japan, [Online]. Available: ⟨https://materials.springer.com/isp/phase-diagram/docs/c_2000114⟩.
[12] M.H. Tsai, R.-C. Tsai, T. Chang, W.-F. Huang, Intermetallic phases in high-entropy alloys: statistical analysis of their prevalence and structural inheritance, Met. (Basel) 9 (247) (2019) 1–18, https://doi.org/10.3390/met9020247
[13] K.H.J. Buschow, P.G. van Engen, Magnetic and magneto-optical properties of heusler alloys based on aluminium and gallium, J. Magn. Magn. Mater. 25 (1) (1981) 90–96, https://doi.org/10.1016/0304-8853(81)90151-7
[14] D.E. Okpalugo, J.G. Booth, Onset of ferromagnetism in 3d-substituted FeAl alloys. I: Ti, V and Cr substitutions, J. Phys. F. Met. Phys. 15 (9) (1985) 2025–2039, https://doi.org/10.1088/0305-4608/15/9/018
[15] D.E. Okpalugo, J.G. Booth, Onset of ferromagnetism in 3d-substituted FeAl alloys. II: Mn and Co substitutions, J. Phys. F. Met. Phys. 15 (9) (1985) 2025–2039, https://doi.org/10.1088/0305-4608/15/9/018
[16] P.J. Barron, A.W. Carruthers, J.W. Fellowes, N.G. Jones, H. Dawson, E.J. Pickering, Towards V-based high-entropy alloys for nuclear fusion applications, Scr. Mater. 176 (2020) 12–16, https://doi.org/10.1016/j.scriptamat.2019.09.028
[17] M.H. Tsai, K.Y. Tsai, C.W. Tsai, C. Lee, C.C. Juan, J.W. Yeh, Criterion for sigma phase formation in Cr- and V-Containing high-entropy alloys, Mater. Res. Lett. 1 (4) (2013) 207–212, https://doi.org/10.1080/21663831.2013.831382
[18] M.H. Tsai, K.C. Chang, J.H. Li, R.C. Tsai, A.H. Cheng, A second criterion for sigma phase formation in high-entropy alloys, Mater. Res. Lett. 4 (2) (2016) 90–95, https://doi.org/10.1080/21663831.2015.1121168
[19] S. Maier, S. Denis, S. Adam, J.C. Crivello, J.M. Joubert, E. Alleno, Order-disorder transitions in the Fe2VAl Heusler alloy, Acta Mater. 121 (2016) 126–136, https://doi.org/10.1016/j.actamat.2016.08.080

[20] P.A. Ferreirós, P.R. Alonso, G.H. Rubiolo, Coarsening process and precipitation hardening in Fe2AlV-strengthened ferritic Fe76Al12V12 alloy, Mater. Sci. Eng. A 684 (October 2016) (2017) 394–405, https://doi.org/10.1016/j.msea.2016.12.074
[21] P.A. Ferreirós, P.R. Alonso, P.H. Gargano, P.B. Bozzano, H.E. Troiani, A. Baruj, G.H. Rubiolo, Characterization of microstructures and age hardening of Fe 1-2xAlxVx alloys, Intermetallics 50 (2014) 65–78, https://doi.org/10.1016/j.intermet.2014.02.014
[22] K. Mahdouk, J.C. Gachon, Thermodynamic investigation of the aluminum-chromium system, J. Phase Equilibria 21 (2) (2000) 157–166, https://doi.org/10.1361/105497100770340219
[23] A.S. Ilyushin, W.E. Wallace, Structural and magnetic properties of the Fe3-xMnxAl system, J. Solid State Chem. 17 (4) (1976) 385–387, https://doi.org/10.1016/S0022-4596(76)80007-2